Imaging nanoscale Fermi-surface variations in an inhomogeneous superconductor

Imaging nanoscale Fermi surface variations in an inhomogeneous superconductor

W. D. Wise[1], Kamalesh Chatterjee[1], M. C. Boyer[1], Takeshi Kondo[2,1*], T. Takeuchi[2,3], H. Ikuta[2], Zhijun Xu[4], Jinsheng Wen[4], G. D. Gu[4], Yayu Wang[1†] & E. W. Hudson[1]

[1]*Department of Physics, Massachusetts Institute of Technology, Cambridge, MA 02139, USA.*

[2]*Department of Crystalline Materials Science, Nagoya University, Nagoya 464-8603, Japan.*

[3]*EcoTopia Science Institute, Nagoya University, Nagoya 464-8603, Japan.*

[4]*Condensed Matter Physics and Materials Sciences Department, Brookhaven National Laboratory, Upton, NY 11973, USA.*

*Present address: Ames Laboratory and Dept. of Physics and Astronomy, Iowa State University, Ames, IA 50011

[†]Present address: Department of Physics, Tsinghua University, Beijing 100084, China.

Particle-wave duality suggests we think of electrons as waves stretched across a sample, with wavevector *k* proportional to their momentum. Their arrangement in "*k*-space," and in particular the shape of the Fermi surface, where the highest energy electrons of the system reside, determine many material properties. Here we use a novel extension of Fourier transform scanning tunneling microscopy to probe the Fermi surface of the strongly inhomogeneous Bi-based cuprate superconductors. Surprisingly, we find that rather than being globally defined, the Fermi surface changes on nanometer length scales. Just as shifting tide lines expose variations of water height, changing Fermi surfaces indicate strong local doping variations. This discovery, unprecedented in any material, paves the way for an understanding of other inhomogeneous characteristics of the cuprates, like the pseudogap magnitude, and highlights a new approach to the study of nanoscale inhomogeneity in general.

That high temperature superconductors should exhibit nanoscale inhomogeneity is unsurprising. In correlated electron materials, Coulomb repulsion between electrons hinders the formation of a homogeneous Fermi liquid, and complex real space phase separation is ubiquitous[1]. Scanning tunneling microscopy (STM) measurements have revealed significant spectral variations in a number of cuprates including $Bi_2Sr_2CuO_{6+x}$ (Bi-2201)[2] and $Bi_2Sr_2CaCu_2O_{8+x}$ (Bi-2212)[3-5].

This intrinsic inhomogeneity poses challenges to the interpretation of bulk or spatially averaged measurements. For example, angle resolved photoemission spectroscopy (ARPES) is a powerful technique for studying ***k***-space structure in the cuprates[6]. However, ARPES can only provide spatially-averaged results, and uniting these with the nanoscale disordered electronic structure measured by STM remains a formidable task.

Our approach to addressing this issue originates from discoveries by Fourier transform scanning tunneling microscopy (FT-STM), which has emerged as an important tool for studying the cuprates. These studies begin with the collection of a spectral survey, in which differential conductance spectra, proportional to local density of states (LDOS), are measured at a dense array of locations, creating a three dimensional dataset of LDOS as a function of energy and position in the plane. By Fourier transforming constant energy slices of these surveys, referred to as LDOS or conductance maps, FT-STM allows the study of two phenomena linked to the cuprate FS (Fig. 1b). First, non-dispersive wavevectors of the checkerboard-like charge order observed in many cuprates[7-10] are likely connected to the FS-nesting wavevectors near the anti-nodal (π,0) Brillouin zone boundary (e.g. arrow in Fig. 1b)[11]. Second, dispersive quasiparticle interference (QPI) patterns[12-14] originate from elastic scattering of quasiparticles on the Fermi surface near the nodal (π, π) direction[15]. Taken together, these phenomena provide complementary information about the cuprate FS.

However, because these phenomena were previously characterized using Fourier transforms of large LDOS maps containing a wide range of energy gaps and spectra, previous FT-STM mapping of the FS was still spatially-averaged.[16] The atomic scale spatial resolution of STM was not exploited, so connections between FS geometry and local electronic structure went unexamined.

Here we introduce two new STM analysis techniques which allow extraction of a *local* FS. In studies of Bi-2201 and Bi-2212, we find that the cuprate FS varies at the nanometer scale, and that its local geometry correlates strongly with the size of the large, inhomogeneous energy gap that has been extensively studied by STM[4] and which we associate with the pseudogap[2].

We first investigate the spatial dependence of the anti-nodal FS using checkerboard charge order. Our recent study of Bi-2201 showed that the average checkerboard wavevector decreases with increased doping[11]. This trend, inconsistent with many proposed explanations of the checkerboard, matches the doping dependence of the anti-nodal FS-nesting wavevector (Fig. 1b), and led us to conclude that the checkerboard is caused by a FS-nesting induced charge density wave. Here we continue the investigation of the three Bi-2201 dopings considered in our previous work, two underdoped with superconducting transitions at 25 K (UD25) and 32 K (UD32), and one optimally doped with T_C = 35 K (OP35). Although, following convention, we previously reported FT-measured, spatially averaged wavevectors, careful observation of the checkerboard pattern (Fig. 2a) shows that the periodicity changes drastically with position.

One way of analyzing this variation is with a Voronoi diagram. After identifying local peaks of the checkerboard modulation (local maxima in the +10 mV conductance map, identified as red dots in Fig. 2a), we divide the map into cells, each containing points closer to one checkerboard maximum than any other. The square root of the cell size is a measure of the local checkerboard wavelength. We find that this local wavelength is highly correlated with the previously observed gap size inhomogeneity (Fig. 2b,c), with a correlation coefficient of -0.4.

Another method of investigating this relationship between local checkerboard periodicity and gap size is to modify the traditional FT technique by first masking the LDOS map by gap size. This technique is illustrated in Fig. 3. The LDOS map is set to zero everywhere outside a desired gap range and then Fourier transformed to reveal a gap dependent checkerboard wavevector. The result is qualitatively similar to the Fourier transform of the complete map, but the wavevector measured is due solely to the fraction of the sample within the selected range of gap magnitudes. Fourier

transforms of different regions reveal different wavevectors (Fig 3b, c). Consistent with previously reported sample averages,[11] wavevectors increase with gap size (Fig. 3d). We note this trend is not an artifact of mask geometry; rotating the masks, which preserves their geometry while eliminating their relation to the gap map, eliminates the trend of figure 3d, instead simply yielding the sample average wavevector for all maps.

These two independent techniques not only demonstrate the inhomogeneity of the checkerboard wavelength, the likely cause of universally reported short checkerboard correlation lengths[11], but also reveal that the checkerboard wavevector and local gap size are strongly correlated. Between samples, average checkerboard wavevector decreases with increased doping[11], consistent with the decrease of the anti-nodal FS-nesting wavevector (Fig. 1b). The tunneling measured gap size (scaling with pseudogap temperature T* of Fig. 1a) also on average decreases with increased doping. Thus the positive correlation of local gap size and checkerboard wavevector is consistent with a picture in which local FS variations, driven by local doping variations, affect both. Notably, where gap sizes from different samples overlap, so do their checkerboard wavelengths (Fig. 3d), indicating that checkerboard properties are truly set by local rather than sample average properties. We stress that this result is independent of the cause of the checkerboard, and relies only on our previously report of its doping dependence[11].

In order to further investigate this idea we next turn to quasiparticle interference (QPI) studies of slightly overdoped (T_C = 89 K) Bi-2212. The idea behind QPI, pioneered by the Davis group[12-14] and Dung-Hai Lee,[15] is illustrated in Fig. 4a. Interference patterns arising from quasiparticle scattering are dominated by wavevectors connecting ***k***-space points of high density of states. For any given energy, eight such symmetric points exist, all on the FS. The well defined wavevectors (colored lines) of the resultant interference pattern can therefore be used to reconstruct the Fermi surface.

Just as in checkerboard studies, previous work on QPI has yielded spatially averaged results[12-14]. As above, we extend QPI analysis to yield local, gap dependent information. The interference wavevectors (circled in Fig. 4b) found in Fourier transforms of gap masked conductance maps can be inverted to derive a FS[13], now associated with the gap range of the mask. Doing this for two different gap ranges, from 30 mV to 60 mV ($<\Delta> = 37$ mV), and 10 mV to 30 mV ($<\Delta> = 26$ mV), we find distinct shifts in the FS (Fig. 4c). We extend this to the anti-node with checkerboard order, resolvable in Bi-2212 as non-dispersive order at energies above where the QPI signal weakens. Adding in nested anti-nodal FS segments (dashed lines) derived from checkerboard periodicity, we arrive at a nearly complete view of different local Fermi surfaces corresponding to different spatial locations, correlated spatially with different gap sizes. We also plot in Fig. 4c rigid band tight binding Fermi surfaces[17] from two different dopings ($p = 0.10$ and 0.18 as calculated from the pocket area) very similar to the surfaces we derive.

Although ***k***-space variation on nanometer length scales may at first glance seem shocking, upon further reflection this result is not entirely surprising. Raising or lowering a uniformly slanted sea floor near the shore (changing the amount of sea above the floor) changes the position of the shoreline. Analogously, raising or lowering local doping changes the local Fermi surface. McElroy et al. have even demonstrated that the locations of dopant oxygen atoms correlate with local gap size variations[18]. Interestingly, the correlation McElroy *et al*. found was the opposite of what one might at first expect from a local doping picture. While oxygen dopants contribute holes and hence increase the global doping of the sample, they correlate with an *increased* local gap size, consistent with underdoping. This led the authors and others[19] to declare that variation in gap size is unlikely to be charge driven and instead propose variations in local pairing-potential.

The results we report here, however, cannot be explained by pairing-potential inhomogeneity. Instead, local doping variations appear most consistent with our results. Although McElroy *et al*. suggest that these variations cannot be explained by hole accumulation models, Zhou *et al*. claim that they have missed the oxygen atoms responsible for inhomogeneity[20]. Alternatively, local doping variations could be driven by dopant generated strain. This would also explain the correlation of gap variations with the strain-associated structural supermodulation in Bi-2212[21].

Regardless of the exact cause of these local doping variations, they can explain several previous results. Perhaps the clearest examples consist of recent STM results from the Yazdani group showing that the gap closing temperature varies spatially, scaling with local gap size,[5] and that both are correlated with higher temperature electronic structure[22]. Those results are unsurprising given the local Fermi surface variations we report here.

Considering the nature of the Fermi surface variations in detail, we find that the locally determined Fermi surfaces converge near the nodes while they are strongly inhomogeneous in the anti-nodes (Fig. 4c). This could explain the ARPES-measured dichotomy of coherent nodal / incoherent anti-nodal quasiparticle excitations found in a variety of cuprates.[6,23] This differentiation is strongest in underdoped samples which could also arise from the inhomogeneity we report here. ARPES sums signal from differently doped regions; as more highly doped regions yield higher signal, ARPES will overemphasize them. Coupled with the observation that the width of the gap (and hence doping) distribution scales with mean gap size[24], and is thus smaller in overdoped than underdoped samples, inhomogeneity should have a stronger effect on ARPES measurements in underdoped than in overdoped samples. This effect is particularly apparent in Bi-2201, which is more inhomogeneous than Bi-2212.[2]

Despite the success of this interpretation, some outstanding questions remain. The model curves[17] of Fig. 4c suggest that the effective band energy may shift by as much as 20 mV between different regions of the sample. This shift would lead to strong scattering, even in the nodal direction. However, aside from the reasonable match to our extracted Fermi surfaces, there is no reason to believe that this global average-extracted rigid band model should completely describe the local Fermi surfaces. For example, our extracted Fermi surfaces appear closer in the nodal region than the model surfaces.

Another question concerns a homogeneous gap we have reported.[2] The large, inhomogeneous gap discussed throughout this paper is probably more accurately termed the pseudogap, while we identified as the superconducting gap a second, relatively homogeneous smaller gap which opens at T_C. One might imagine that superconductivity, as characterized by size of the superconducting gap, should be as strongly affected by inhomogeneous local doping as the pseudogap. This is not what we have observed[2]. One explanation is that doping dependence differences make inhomogeneity affect the pseudogap more than the superconducting gap (the pseudogap, scaling with T*, changes more than the superconducting gap, scaling with T_C). Another explanation may lie in their momentum space distribution. Raman spectroscopy[25] and ARPES[26,27] results indicate that the superconducting gap is most strongly associated with near-nodal states, while the pseudogap arises near the anti-nodes. As noted above, the nodal region is significantly more homogeneous than the antinodal, and hence could lead to more homogeneous superconducting than pseudogap properties.

This interpretation also points towards an explanation of bulk measurement results. Although several are suggestive of nanoscale inhomogeneity[4], including neutron measurements of the magnetic resonance peak width[28], thermodynamic measurements appear inconsistent with strong inhomogeneity[29]. These measurements, however, are most sensitive to the nature of the *superconducting* gap and the low energy density of

states, both of which appear homogeneous. Undoubtedly these homogeneous properties relate to the homogeneity of the near nodal Fermi surface. Nonetheless, they are remarkable given the strong inhomogeneity we report here.

Inhomogeneity of doping or charge is common in many materials, and leads naturally to the idea of nanoscale Fermi surface variation. This work is, to our knowledge, the first attempt to characterize these variations, and raises the question of whether a Fermi surface, typically thought of as a bulk property, can be meaningfully defined inside nanometer sized domains. Although our experimental results appear consistent with this picture, further experimental and theoretical work are needed to determine at what point a k-space description such as this stops being useful.

References

[1] Dagotto, E., Complexity in strongly correlated electronic systems. *Science* **309**, 257-262 (2005).

[2] Boyer, M. C. *et al.*, Imaging the two gaps of the high-temperature superconductor $Bi_2Sr_2CuO_{6+x}$. *Nature Phys.* **3**, 802-806 (2007).

[3] Howald, C., Fournier, P., and Kapitulnik, A., Inherent inhomogeneities in tunneling spectra of $Bi_2Sr_2CaCu_2O_{8-x}$ crystals in the superconducting state. *Phys. Rev. B* **64**, 100504 (2001).

[4] Lang, K. M. *et al.*, Imaging the granular structure of high-T_C superconductivity in underdoped $Bi_2Sr_2CaCu_2O_{8+\delta}$. *Nature* **415**, 412-416 (2002).

[5] Gomes, K. K. *et al.*, Visualizing pair formation on the atomic scale in the high-Tc superconductor $Bi_2Sr_2CaCu_2O_{8+\delta}$. *Nature* **447**, 569-572 (2007).

[6] Damascelli, A., Hussain, Z., and Shen, Z.-X., Angle-resolved photoemission studies of the cuprate superconductors. *Rev. Mod. Phys.* **75**, 473-541 (2003).

[7] Howald, C., Eisaki, H., Kaneko, N., Greven, M., and Kapitulnik, A., Periodic density-of-states modulations in superconducting $Bi_2Sr_2CaCu_2O_{8+\delta}$. *Phys. Rev. B* **67**, 014533 (2003).

[8] Vershinin, M. *et al.*, Local Ordering in the Pseudogap State of the High-T_C Superconductor $Bi_2Sr_2CaCu_2O_{8+\delta}$. *Science* **303**, 1995-1998 (2004).

[9] Hanaguri, T. *et al.*, A `checkerboard' electronic crystal state in lightly hole-doped $Ca_{2-x}Na_xCuO_2Cl_2$. *Nature* **430**, 1001-1005 (2004).

[10] McElroy, K. *et al.*, Coincidence of checkerboard charge order and antinodal state decoherence in strongly underdoped superconducting $Bi_2Sr_2CaCu_2O_{8+\delta}$. *Phys. Rev. Lett.* **94**, 197005 (2005).

[11] Wise, W. D. *et al.*, Charge-density-wave origin of cuprate checkerboard visualized by scanning tunnelling microscopy. *Nature Phys.* **4**, 696-699 (2008).

[12] Hoffman, J. E. *et al.*, Imaging quasiparticle interference in $Bi_2Sr_2CaCu_2O_{8+\delta}$. *Science* **297**, 1148-1151 (2002).

[13] McElroy, K. *et al.*, Relating atomic-scale electronic phenomena to wave-like quasiparticle states in superconducting $Bi_2Sr_2CaCu_2O_{8+\delta}$. *Nature* **422**, 592-596 (2003).

[14] Hanaguri, T. *et al.*, Quasiparticle interference and superconducting gap in $Ca_{2-x}Na_xCuO_2Cl_2$. *Nature Phys.* **3**, 865-871 (2007).

[15] Wang, Q.-H. and Lee, D.-H., Quasiparticle scattering interference in high-temperature superconductors. *Phys. Rev. B* **67**, 020511 (2003).

[16] Del Maestro, A., Rosenow, B., and Sachdev, S., From stripe to checkerboard ordering of charge-density waves on the square lattice in the presence of quenched disorder. *Phys. Rev. B* **74**, 024520 (2006).

[17] Norman, M. R., Randeria, M., Ding, H., and Campuzano, J. C., Phenomenological models for the gap anisotropy of $Bi_2Sr_2CaCu_2O_8$ as measured by angle-resolved photoemission spectroscopy. *Phys. Rev. B* **52**, 615-622 (1995).

[18] McElroy, K. *et al.*, Atomic-scale sources and mechanism of nanoscale electronic disorder in $Bi_2Sr_2CaCu_2O_{8+\delta}$. *Science* **309**, 1048-1052 (2005).

[19] Nunner, T. S., Andersen, B. M., Melikyan, A., and Hirschfeld, P. J., Dopant-Modulated Pair Interaction in Cuprate Superconductors. *Phys. Rev. Lett.* **95**, 177003 (2005).

[20] Zhou, S., Ding, H., and Wang, Z., Correlating Off-Stoichiometric Doping and Nanoscale Electronic Inhomogeneity in the High-T_c Superconductor $Bi_2Sr_2CaCu_2O_{8+\delta}$. *Phys. Rev. Lett.* **98**, 076401 (2007).

[21] Slezak, J. A. *et al.*, Imaging the impact on cuprate superconductivity of varying the interatomic distances within individual crystal unit cells. *PNAS* **105**, 3203-3208 (2008).

[22] Pasupathy, A. N. *et al.*, Electronic Origin of the Inhomogeneous Pairing Interaction in the High-Tc Superconductor $Bi_2Sr_2CaCu_2O_{8+\delta}$. *Science* **320**, 196-201 (2008).

[23] Zhou, X. J. *et al.*, Dichotomy between nodal and antinodal quasiparticles in underdoped $(La_{2-x}Sr_x)CuO_4$ superconductors. *Phys. Rev. Lett.* **92**, 187001 (2004).

[24] Alldredge, J. W. *et al.*, Evolution of the electronic excitation spectrum with strongly diminishing hole density in superconducting $Bi_2Sr_2CaCu_2O_{8+\delta}$. *Nat Phys* **4**, 319-326 (2008).

[25] Le Tacon, M. *et al.*, Two energy scales and two distinct quasiparticle dynamics in the superconducting state of underdoped cuprates. *Nature Phys.* **2**, 537-543 (2006).

[26] Tanaka, K. *et al.*, Distinct Fermi-Momentum-Dependent Energy Gaps in Deeply Underdoped Bi2212. *Science* **314**, 1910-1913 (2006).

[27] Kondo, T., Takeuchi, T., Kaminski, A., Tsuda, S., and Shin, S., Evidence for Two Energy Scales in the Superconducting State of Optimally Doped $(Bi,Pb)_2(Sr,La)_2CuO_{6+\delta}$. *Phys. Rev. Lett.* **98**, 267004 (2007).

[28] Fauqué, B. *et al.*, Dispersion of the odd magnetic resonant mode in near-optimally doped $Bi_2Sr_2CaCu_2O_{8+\delta}$. *Phys. Rev. B* **76**, 214512 (2007).

[29] Loram, J. W. and Tallon, J. L., Thermodynamic transitions in inhomogeneous cuprate superconductors. Preprint at < http://arxiv.org/abs/cond-mat/0609305 >.

Acknowledgements

We thank A.V. Balatsky, N. Gedik, J.E. Hoffman, K.M. Lang, P.A. Lee, Y. Lee, T. Senthil and Z. Wang for helpful comments. This research was supported in part by a Cottrell Scholarship awarded by the Research Corporation, by the MRSEC and CAREER programs of the NSF, and by DOE.

Author Contributions

WDW, KC and MCB shared equal responsibility for most aspects of this project from instrument construction through data collection and manuscript preparation. WDW performed a majority of the analysis. TK grew the Bi-2201 samples and helped refine the STM. TT and HI contributed to Bi-2201

sample growth. ZX, JW and GDG contributed to Bi-2212 sample growth. YW contributed to analysis and manuscript preparation. EWH advised.

Correspondence and requests for materials should be addressed to EWH (ehudson@mit.edu).

Figure Captions

Figure 1. **Phase diagram and Fermi surface topology of the cuprates**. (a) A minimal generic phase diagram of the high temperature superconductors shows a superconducting transition temperature T_C which is parabolic with doping, peaking at optimal doping, while the pseudogap temperature T* – and the proportional pseudogap magnitude Δ_{PG} – decrease nearly linearly with doping. (b) The hole-doped cuprate Fermi surface is typically seen as hole-like, closing around empty states centered at (π,π), rather than filled states centered at (0,0). Moving from optimally doped (solid line) to underdoped (dashed) materials, the hole pockets shrink. This increases the length of the nesting vector (arrow) near the anti-node.

Figure 2. **Local variations of the Bi-2201 checkerboard**. (a) Conductance map (E = +10 mV slice of a 400 pixel, 600 Å spectral survey) of T_C = 32 K underdoped Bi-2201 shows a spatially varying checkerboard charge modulation (upper left). Voronoi cells, associated with checkerboard maxima (red dots) and colored to indicate their area, allow determination of local wavelength. (b) Traditional gap map of the same area shows well known variations of gap size Δ. (c) Spectra from the survey (sorted, averaged and colored by gap size, and shifted vertically for clarity) highlight the remarkable low energy homogeneity in the presence of strong higher energy inhomogeneity. Spectral survey parameters: I_{set} = 400 pA, V_{sample} = -200 mV.

Figure 3. **Gap masked Fourier transform measurements of the Bi-2201 checkerboard**. (a) Using the gap map of Fig. 2b we mask the conductance

map of Fig. 2a, zeroing out (shading pink) data with gaps outside a desired range, here Δ = 40 mV to 55 mV. (b,c) Fourier transforms of the masked data (with (b) $<\Delta>$ = 30 mV and (c) $<\Delta>$ = 60 mV) show checkerboard wavevectors, whose length can be compared to the atomic periodicity, that shift with gap masking range. (d) Checkerboard wavevectors for this sample (green triangles) as well as optimally doped 35 K (orange square) and underdoped 25 K (blue circles) samples. Overlaid are large area averages from our previous work.[11] Error bars indicate standard deviation of gap range used (horizontal) and FFT peak fit accuracy (vertical). Gap ranges are non-uniform as they are selected to ensure roughly the same coverage in each mask.

Figure 4. **Quasiparticle interference derived local FS in Bi-2212**. (a) A schematic of the FS (solid line) in the first Brillouin zone, shows symmetry, leading to an eight fold replication of any points at which the density of states peak (e.g. circles). Scattering between quasiparticles at these points lead to a set of interference wavevectors (arrows), corresponding to peaks in interference maps like (b) a Fourier transform of a 600 Å, 400 pixel, E = 12 mV conductance map of 89 K OD Bi-2212. The positions of these peaks (defined in terms of the atomic wavevector circled in black) uniquely define a position in k-space on the FS. Fitting interference peaks in a series of FFT maps at various energies from two different masks of the same data leads to (c), two different "local Fermi surfaces" (solid symbols with error bars indicating standard deviation for values obtained from different interference peaks). Dashed lines, obtained from checkerboard determined nesting wavevectors, extend the determined FS to the anti-node. Solid lines are Fermi surfaces from a rigid band, tight binding model[17] at two different dopings, p = 0.10 and 0.18.

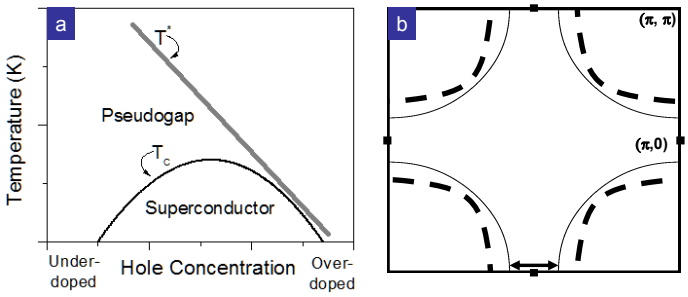

Wise, Figure 1

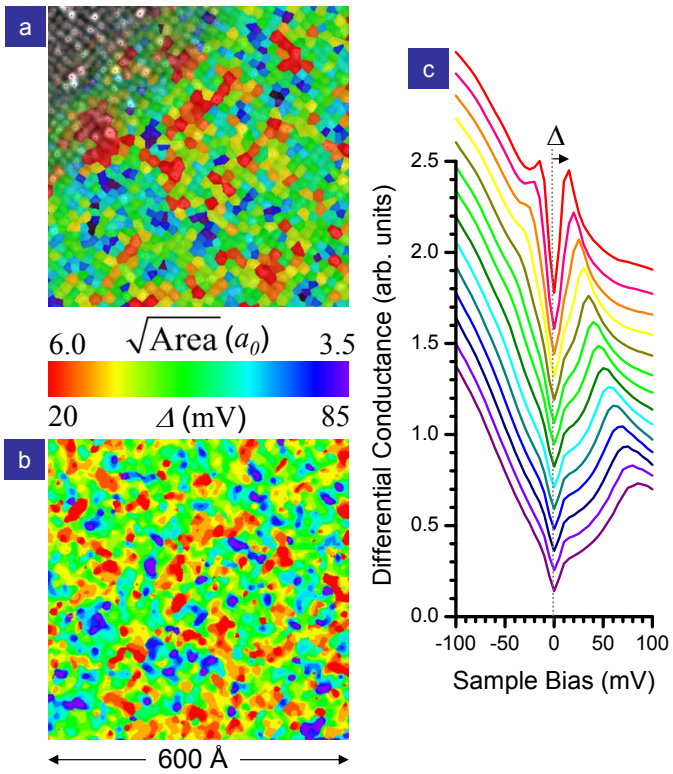

Wise, Figure 2

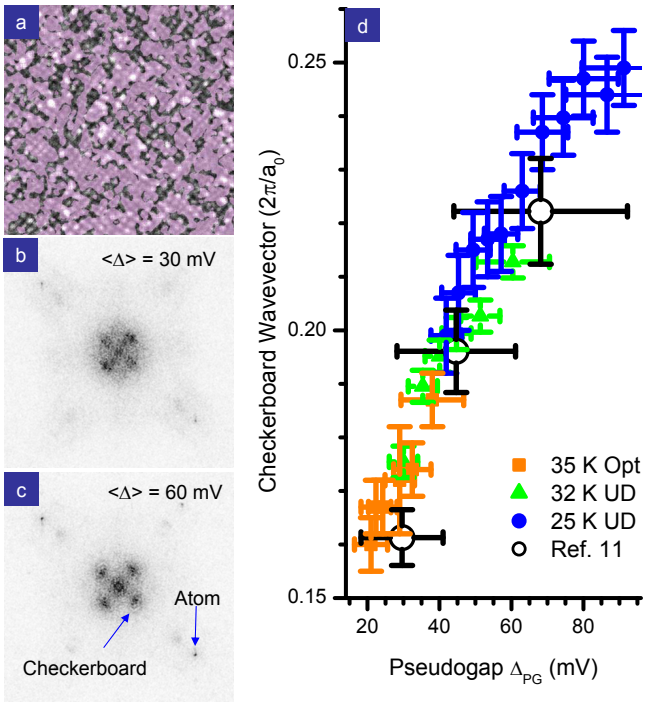

Wise, Figure 3

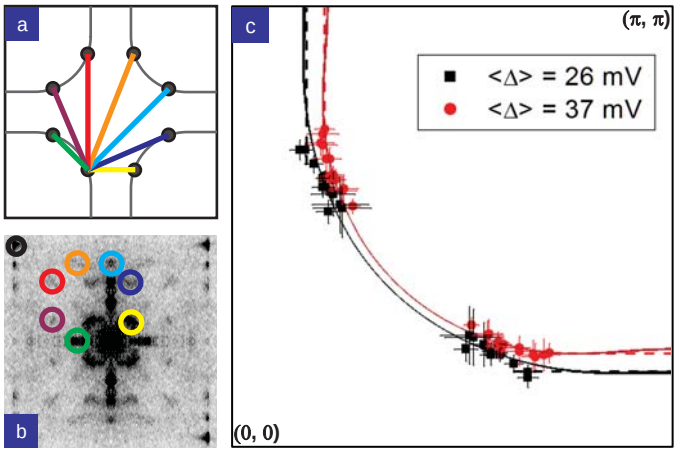
a
b
c
(π, π)
<Δ> = 26 mV
<Δ> = 37 mV
(0, 0)

Imaging nanoscale Fermi surface variations in an inhomogeneous superconductor: Supplement

In this work we use the technique of Fourier transforming masked conductance maps to extract gap dependence of both the checkerboard wavelength and quasiparticle interference patterns. In this supplement we address some possible concerns about the results derived with this novel technique.

A first question is whether the geometry of the masks themselves could be responsible for the derived wavevector shifts. As noted in the text, we can test for such a masking effect by rotating masks before applying them to the conductance map, preserving mask geometry while removing the correlation between masks and the gap map. If mask geometry is responsible for the observed variations, then these variations should also be observed in Fourier transforms of data masked with rotated masks. If not, then rotated masks should yield non-dispersing (sample average) results. We show results of this test applied to $\langle\Delta\rangle$ = 30 mV and 60 mV masks of data from a 32 K UD sample in Fig. S1. While properly masked data shows strong gap dependent dispersion, as shown previously in Fig. 3b and 3c, rotated masks produce nearly indistinguishable transforms S1g and S1h.

Thus we conclude that map geometry is not responsible for the gap dependent wavevectors we report here, in either the checkerboard or quasiparticle interference results. Next, we test whether map geometry plays a role in the width of the Fourier peaks. We simulate an ideal (monochromatic) checkerboard, and mask and Fourier transform it with the 60 mV mask of Fig S1b. While the Fourier transform (FT) of the unmasked simulation shows four very sharp peaks (Fig. S2b), that of the masked simulation (Fig. S2d), shows broadened peaks, with width comparable to that of the data itself (Fig. S2f), with a caveat. Line cuts through the peaks (Fig. S2i) show that the

masked simulation results (black squares) closely resemble the data (red squares), with the presence of an additional superimposed sharp peak. This discrepancy is due to the difference in correlation lengths of simulation and data. Measurement of domain sizes in gap maps show that domains typically have a diameter of 30 Å to 40 Å, or about $8a_0$ to $10a_0$. Perhaps surprisingly, this domain size seems independent of gap size and doping, and is the same in Bi-2201 and Bi-2212. Their size places a natural limit on the correlation length of the observed checkerboard pattern, which translates into a finite peak width, as shown in Fig. 2i. Although the mask reflects this domain size, and hence leads to the same low amplitude shape in the simulated results, because the simulation is coherent it yields a sharp central peak, with width limited by the overall map size (600 Å). The effect of 30 Å domains in the data may be further compared to masking the simulation with a single 30 Å diameter circle. Although the amplitude of the transform is smaller, due to the smaller area being transformed, the width is comparable.

The importance of the correlation length of the underlying (unmasked) data may be observed in Fig. S3, where we show the effects of simulated phase disorder in our ideal checkerboard. While the FT of the ideal checkerboard shows a sharp central peak (black curve), as we introduce disorder by randomizing the phase in adjacent domains, the reduced correlation length causes the amplitude of the central peak to decrease as it broadens. Simulated phase disorder on a 30 Å length scale (cyan) effectively reproduces the data (red).

In short, the peak width is not an artifact of map geometry, but rather reflects the inherent domain size and hence limited correlation length of gap dependent periodic modulations, such as the checkerboard and quasiparticle interference patterns. This has the related benefit that the exact mask used does not affect the gap size-wavevector relation we here report, as long as the mask captures the gap domains of interest. We

choose to make our masks cover a fixed fraction of the field of view, but what fraction is used plays no measureable role in the results.

Finally, because of the clear relationship between gap magnitude and checkerboard periodicity, one might ask whether conductance variations associated with gap inhomogeneity could actually create the checkerboard modulation, or at least perturb its apparent wavelength. As we show in Fig. 2c, there are significant conductance variations associated with gap inhomogeneity. Their position dependence, however, is quite interesting, as we show in Fig. S4. Here we calculate the average conductance for four different types of regions in the sample, namely on and off of checkerboard peaks in Δ = 30 mV and 60 mV domains. Although low energy conductance is relatively homogeneous, the contrast at 10 mV, where the checkerboard is most clearly imaged, is clearly much higher between peaks and troughs (on and off the maxima) than it is between different gap regions. That is to say, conductance changes due to gap inhomogeneity are a small perturbation to those caused by the checkerboard modulation itself and hence cannot be concluded to cause the wavelength variations we report here. On a related note, although we use a typical STM normalization in reporting our data – fixing the integral of the differential conductance from 0 mV to some large voltage bias, here -100 mV – the results presented here aren't particularly sensitive to this normalization. For example, if one instead chooses to fix the conductance in the wings (force the curves in Fig. S4 to coincide at the left edge of the figure) the same dominance of checkerboard position over gap variation is still found.

Figure Captions

Figure S1. **Testing the effects of mask geometry**. (a, b) Masks used for the 32K UD map of Fig. 2 and 3, where spectra taken in white areas show $<\Delta>$ = 30 mV and 60 mV respectively. (c, d) Fourier transforms (FTs) of those masks show no obvious structure at any particular wavelength, but instead highlight the low frequency inhomogeneity present in the sample. (e, f) Applying these masks to the map (by setting data in black regions to zero) and taking an FT yields the results of Figs. 3b and 3c, reproduced here. (g, h) If the masks are first rotated 90º, breaking the correlation between mask and gap, the resultant FTs are similar to each other and the sample average.

Figure S2. **Mask geometry and peak width**. (a) A simulated checkerboard map, with a $4.7a_0$ wavelength (corresponding to the 0.213 ($2\pi/a_0$) wavevector found for the $<\Delta>$ = 60 mV masked 32K UD data). The map is 400 pixels over 600 Å, to match the data of Fig. S1. (b) The Fourier transform of this simulation shows 4 narrow peaks, as expected. (c, d) Masking the simulation with the $<\Delta>$ = 60 mV mask of Fig. S1b broadens the peaks, similar to the peaks in the data (e, f). (g, h) A single 30 Å diameter circle masking the simulation yields a similar width, although the amplitude is reduced and hence (h) is multiplied by 10 before being shown in the same color scale as (b, d, f). (i) Line cuts through the Fourier peaks (as shown by the short lines on d, f, and h) show the similar widths of data and simulation, due to the size of the gap domains and hence mask features.

Figure S3. **Correlation length effects**. (a,b) Simulated checkerboard maps with the same parameters of Fig. S2, with the addition of phase disorder with 75 Å and 30 Å domains respectively. (c) Line cuts through Fourier transforms of maps such as a & b, masked and analyzed as in Fig. S2, demonstrate the importance of the correlation length of the checkerboard in determining the amplitude and width of the central peak. The use of (b) 30 Å domains (cyan) effectively simulates the data (red).

Figure S4. **Position and gap dependent conductance**. Using the 32 K UD spectral survey analyzed throughout this paper, data is segregated by gap size as well as by whether it lies on a peak (the pixel lying at a checkerboard conductance maximum) or in a trough (the pixel wide boundary region between the Voronoi cells shown in Fig. 2a). The average of such spectra for two gap sizes, Δ = 30 mV (black) and 60 mV (red), vary much more significantly with position, that is between peak (solid) and trough (dashed), than with gap size.

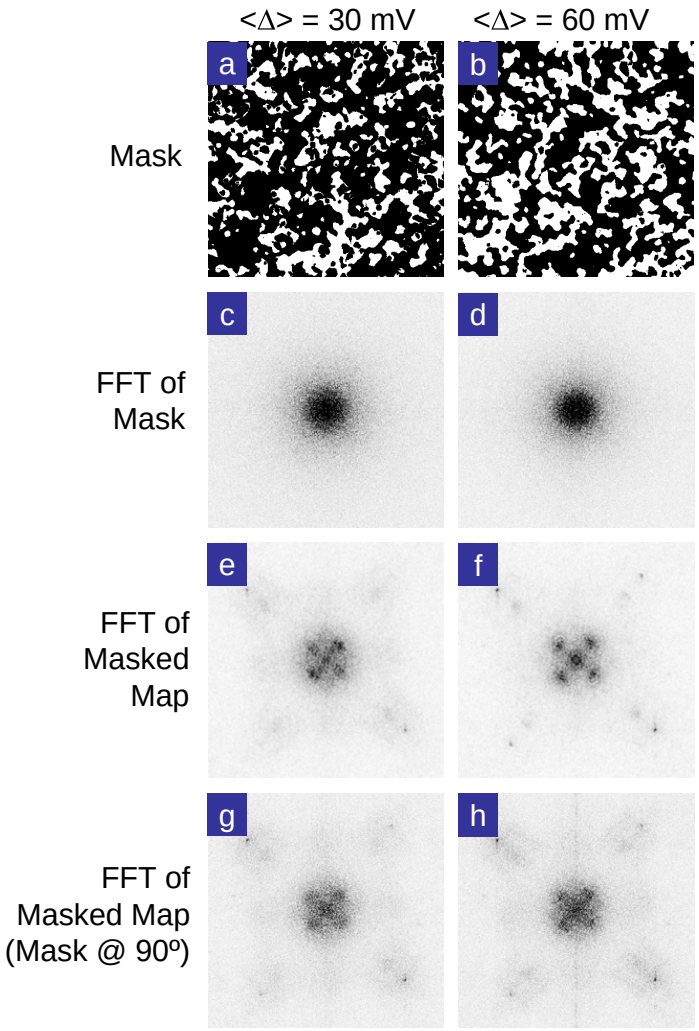

Wise et al., Fig. S1

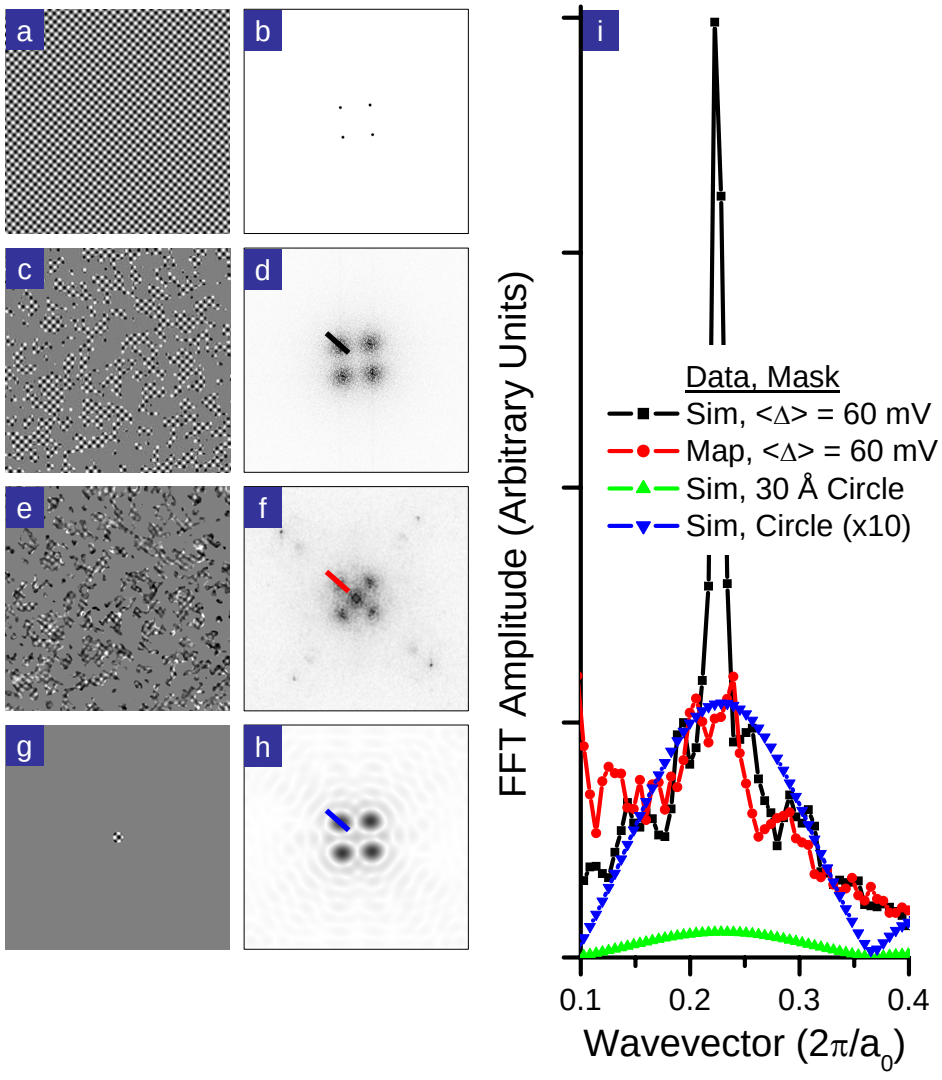

Wise et al., Fig. S2

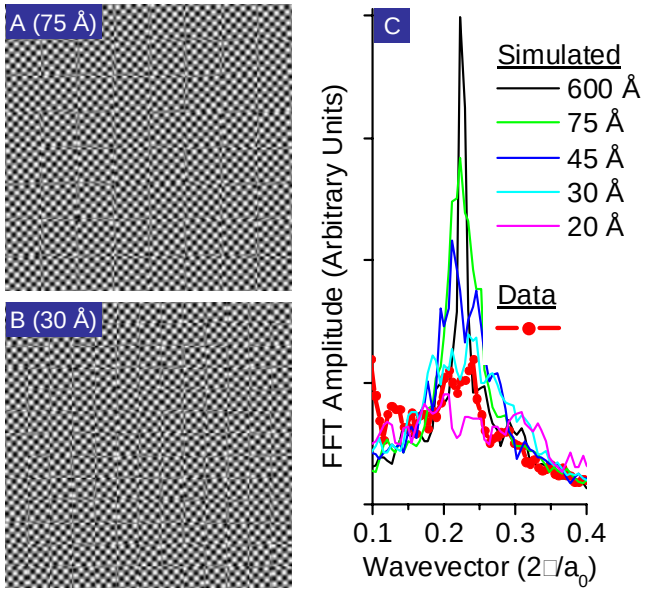

Wise et al., Fig. S3

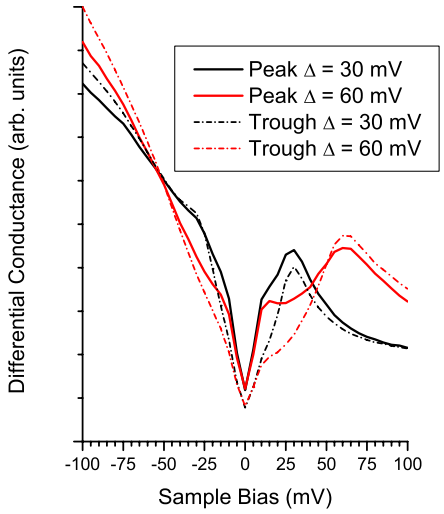
Peak Δ = 30 mV
Peak Δ = 60 mV
Trough Δ = 30 mV
Trough Δ = 60 mV
Differential Conductance (arb. units)
-100 -75 -50 -25 0 25 50 75 100
Sample Bias (mV)